

A faster algorithm for smoothed particle hydrodynamics with radiative transfer in the flux-limited diffusion approximation

Stuart C. Whitehouse¹, Matthew R. Bate¹ and Joe J. Monaghan²*

1. School of Physics, University of Exeter, Stocker Road, Exeter EX4 4QL

2. School of Mathematical Sciences, Monash University, Clayton 3800, Australia

Accepted for publication in MNRAS

ABSTRACT

We describe a new, faster implicit algorithm for solving the radiation hydrodynamics equations in the flux-limited diffusion approximation for smoothed particle hydrodynamics. This improves on the method elucidated in Whitehouse & Bate by using a Gauss-Seidel iterative method rather than iterating over the exchange of energy between pairs of particles. The new algorithm is typically many thousands of times faster than the old one, which will enable more complex problems to be solved. The new algorithm is tested using the same tests performed by Turner & Stone for ZEUS-2D, and repeated by Whitehouse & Bate.

Key words: hydrodynamics – methods: numerical – radiative transfer.

1 INTRODUCTION

Smoothed particle hydrodynamics (SPH) is a Lagrangian method introduced by Lucy (1977) and Gingold & Monaghan (1977) that is frequently used for simulating astrophysical fluid problems, for example for star and galaxy formation and supernovae. However, it has also been used outside of astrophysics, for example for the modelling of tsunami and volcanoes (see Monaghan 1992, for a review).

SPH is normally used to model hydrodynamics, with the inclusion of self-gravity in astrophysical contexts. The smoothing length, which may be variable both in space and in time, enables SPH to naturally adapt its resolution to reflect the local density distribution. However, in many astrophysical situations radiation transport is also an important element. Various attempts have been made to include radiation transport into SPH. Lucy (1977) made the first foray into this field, using the diffusion approximation to examine the fission of protostars. Brookshaw (1985, 1986) also used radiative transfer in the diffusion approximation, modelling stars with entropy gradients. Oxley & Woolfson (2003) combined SPH with a Monte-Carlo radiation transport method. Viau, S. (1995) and Bastien et al. (2004) presented an implicit scheme for the diffusion approximation. Finally, Whitehouse & Bate (2004) developed an implicit scheme for two-temperature (gas and radiation) radiative transfer in the flux-limited diffusion approximation.

In this paper we describe a significant improvement to the method of Whitehouse & Bate (2004), namely the implementation of an implicit algorithm which is many thousands of times faster, but still models the same physics. Section 2 begins by summarising the origins of the flux-limited diffusion approximation, and continues into a brief overview of the explicit SPH equations derived by Whitehouse & Bate (2004), before describing in detail the new method. Section 3 describes the tests we performed to validate this code. These test results should be compared with those of Turner & Stone (2001) and Whitehouse & Bate (2004).

2 METHOD

In a frame co-moving with the fluid, and assuming local thermal equilibrium (LTE), the equations governing the time-evolution of radiation hydrodynamics (RHD) are

$$\frac{D\rho}{Dt} + \rho \nabla \cdot \mathbf{v} = 0, \quad (1)$$

$$\rho \frac{D\mathbf{v}}{Dt} = -\nabla p + \frac{\chi_F \rho}{c} \mathbf{F}, \quad (2)$$

* E-mail: scw@astro.ex.ac.uk, mbate@astro.ex.ac.uk, joe.monaghan@sci.monash.edu.au

$$\rho \frac{D}{Dt} \left(\frac{E}{\rho} \right) = -\nabla \cdot \mathbf{F} - \nabla \mathbf{v} : \mathbf{P} + 4\pi\kappa_p \rho B - c\kappa_E \rho E, \quad (3)$$

$$\rho \frac{D}{Dt} \left(\frac{e}{\rho} \right) = -p \nabla \cdot \mathbf{v} - 4\pi\kappa_p \rho B + c\kappa_E \rho E, \quad (4)$$

$$\frac{\rho}{c^2} \frac{D}{Dt} \left(\frac{\mathbf{F}}{\rho} \right) = -\nabla \cdot \mathbf{P} - \frac{\chi_F \rho}{c} \mathbf{F} \quad (5)$$

(Mihalas & Mihalas 1984; Turner & Stone 2001). In these equations, $D/Dt \equiv \partial/\partial t + \mathbf{v} \cdot \nabla$ is the convective derivative. The symbols ρ , e , \mathbf{v} and p represent the material mass density, energy density, velocity, and scalar isotropic pressure respectively. The total frequency-integrated radiation energy density, momentum density (flux) and pressure tensor are represented by E , \mathbf{F} , and \mathbf{P} , respectively.

A detailed explanation of the flux-limited diffusion approximation to the above equations is given by Turner & Stone (2001). Here we simply summarise the main points. The assumption of LTE allows the rate of emission of radiation from the matter in equations 3 and 4 to be written as the Planck function, B . Equations 2 to 5 have been integrated over frequency, leading to the flux mean total opacity χ_F , and the Planck mean and energy mean absorption opacities, κ_p and κ_E . In this paper, the opacities are assumed to be independent of frequency so that $\kappa_p = \kappa_E$ and the subscripts may be omitted. The total opacity, χ , is the sum of components due to the absorption κ and the scattering σ .

The equations of RHD may be closed by an equation of state, specifying the gas pressure, the addition of constitutive relations for the Planck function and opacities, and an assumption about the relationship between the angular moments of the radiation field.

In this paper, we use an ideal equation of state for the gas pressure $p = (\gamma - 1)u\rho$, where $u = e/\rho$ is the specific energy of the gas. Thus, the temperature of the gas is $T_g = (\gamma - 1)\mu u/R_g = u/c_v$, where μ is the dimensionless mean particle mass, R_g is the gas constant and c_v is the specific heat capacity of the gas. The Planck function is given by $B = (\sigma_B/\pi)T_g^4$, where σ_B is the Stefan-Boltzmann constant. The radiation energy density also has an associated temperature T_r from the equation $E = 4\sigma_B T_r^4/c$.

For an isotropic radiation field $\mathbf{P} = \frac{1}{3}E$. The Eddington approximation assumes this relation holds everywhere and implies that, in a steady state, equation 5 becomes

$$\mathbf{F} = -\frac{c}{3\chi\rho} \nabla E. \quad (6)$$

This expression gives the correct flux in optically thick regions, where $\chi\rho$ is large. However in optically thin regions where $\chi\rho \rightarrow 0$ the flux tends to infinity whereas in reality $|\mathbf{F}| \leq cE$. Flux-limited diffusion solves this problem by limiting the flux in optically thin environments to always obey this inequality. Levermore & Pomraning (1981) wrote the radiation flux in the form of Fick's law of diffusion as

$$\mathbf{F} = -D\nabla E, \quad (7)$$

with a diffusion constant given by

$$D = \frac{c\lambda}{\chi\rho}. \quad (8)$$

The dimensionless function $\lambda(E)$ is called the flux limiter. The radiation pressure tensor may then be written in terms of the radiation energy density as

$$\mathbf{P} = fE, \quad (9)$$

where the components of the Eddington tensor, \mathbf{f} , are given by

$$\mathbf{f} = \frac{1}{2}(1 - f)\mathbf{I} + \frac{1}{2}(3f - 1)\hat{\mathbf{n}}\hat{\mathbf{n}}, \quad (10)$$

where $\hat{\mathbf{n}} = \nabla E/|\nabla E|$ is the unit vector in the direction of the radiation energy density gradient and the dimensionless scalar function $f(E)$ is called the Eddington factor. The flux limiter and the Eddington factor are related by

$$f = \lambda + \lambda^2 R^2, \quad (11)$$

where R is the dimensionless quantity $R = |\nabla E|/(\chi\rho E)$.

Equations 7 to 11 close the equations of RHD, eliminating the need to solve equation 5. However, we must still choose an expression for the flux limiter, λ . In this paper, we choose Levermore & Pomraning (1981)'s flux limiter

$$\lambda(R) = \frac{2 + R}{6 + 3R + R^2}, \quad (12)$$

to allow comparison of our results with those of Turner & Stone (2001) and Whitehouse & Bate (2004).

2.1 The explicit method

In Whitehouse & Bate (2004), we described a method by which equations 2 to 4 can be written in SPH formalism. Equation 1 does not need to be solved directly since the density of each particle is calculated using the standard SPH summation over the particle and its neighbours.

We define the specific energy of the gas to be $u = e/\rho$, and that of the radiation to be $\xi = E/\rho$. The explicit equations in one dimension are then

$$\frac{Dv_i}{Dt} = - \sum_{j=1}^N m_j \left(\frac{p_i}{\rho_i^2} + \frac{p_j}{\rho_j^2} + \Pi_{ij} \right) \nabla W(r_{ij}, h_{ij}) - \frac{\lambda_i}{\rho_i} \sum_{j=1}^N m_j \xi_j \nabla W(r_{ij}, h_{ij}), \quad (13)$$

$$\frac{D\xi_i}{Dt} = \sum_{j=1}^N \frac{m_j}{\rho_i \rho_j} c \left[\frac{4 \frac{\lambda_i}{\kappa_i \rho_i} \frac{\lambda_j}{\kappa_j \rho_j}}{\left(\frac{\lambda_i}{\kappa_i \rho_i} + \frac{\lambda_j}{\kappa_j \rho_j} \right)} \right] \left(\rho_i \xi_i - \rho_j \xi_j \right) \frac{\nabla W_{ij}}{r_{ij}} - (\nabla \cdot \mathbf{v})_i f_i \xi_i - ack_i \left(\frac{\rho_i \xi_i}{a} - \left(\frac{u_i}{c_{v,i}} \right)^4 \right), \quad (14)$$

$$\frac{Du_i}{Dt} = \frac{1}{2} \sum_{j=1}^N \left(\frac{p_i}{\rho_i^2} + \frac{p_j}{\rho_j^2} + \Pi_{ij} \right) m_j \mathbf{v}_{ij} \cdot \nabla W_{ij} + ack_i \left(\frac{\rho_i \xi_i}{a} - \left(\frac{u_i}{c_{v,i}} \right)^4 \right), \quad (15)$$

where $a = 4\sigma_B/c$, m_i is the mass of SPH particle i , $\mathbf{r}_{ij} = \mathbf{r}_i - \mathbf{r}_j$ is the difference in positions between particles i and j , $\mathbf{v}_{ij} = \mathbf{v}_i - \mathbf{v}_j$, and $W_{ij} = W(r_{ij}, h_{ij})$, where W is the standard cubic spline kernel and the mean smoothing length of particles i and j is $h_{ij} = (h_i + h_j)/2$. The smoothing lengths are defined in the same manner as those in Whitehouse & Bate (2004), so each particle has approximately eight neighbours unless otherwise stated.

We use the standard SPH artificial viscosity

$$\Pi_{ij} = \begin{cases} (-\alpha_v c_s \mu_{ij} + \beta_v \mu_{ij}^2) / \rho_{ij} & \text{if } \mathbf{v}_{ij} \cdot \mathbf{r}_{ij} \leq 0, \text{ and} \\ 0 & \text{if } \mathbf{v}_{ij} \cdot \mathbf{r}_{ij} > 0. \end{cases}$$

where $\mu_{ij} = h(\mathbf{v}_i - \mathbf{v}_j) \cdot (\mathbf{r}_i - \mathbf{r}_j) / \left(|\mathbf{r}_i - \mathbf{r}_j|^2 + \eta^2 \right)$, with $\eta^2 = 0.01h^2$ to prevent numerical divergences if particles get too close together. We use $\alpha_v = 1$ and $\beta_v = 2$ unless stated otherwise. In equation 14 the first term on the right hand side is the diffusion term, the second is the work done on the radiation field (in one dimension), and the final term allows energy transfer between the radiation and the gas. In equation 15 the energy transfer term occurs with opposite sign, while the remaining term is the symmetric SPH expression for work and viscous dissipation done on the gas when the thermodynamic variable of integration is energy.

We also tested a supercritical shock (see section 3.4) with an implicit method derived from the asymmetric variant of the work term in equation 15

$$\frac{Du_i}{Dt} = \sum_{j=1}^N \left(\frac{p_i}{\rho_i^2} + \frac{1}{2} \Pi_{ij} \right) m_j \mathbf{v}_{ij} \cdot \nabla W_{ij} + ack_i \left(\frac{\rho_i \xi_i}{a} - \left(\frac{u_i}{c_{v,i}} \right)^4 \right). \quad (16)$$

The two forms of the gas energy equation gave results that differed by two per cent or less. All results presented in this paper use the symmetric version.

2.2 Implicit method

The implicit method for solving the energy equations described by Whitehouse & Bate (2004) calculated the gas work and viscous terms and the diffusion term as an interaction between pairs of particles, subtracting energy from one particle and adding it to another. The radiation pressure term was added to ξ , while the interaction term between the gas and the radiation was calculated by the solution of a quartic equation. The required timestep dt was split into N substeps and the particles swept over. This solution was then compared to that with $2N$ substeps. If the fractional error between the two solutions was not less than a specified tolerance, the number of substeps was doubled until the required tolerance was reached.

The new formulation uses a Gauss-Seidel method to iterate towards the solution of the system of equations. We use a backwards Euler implicit method rather than the trapezoidal method used in Whitehouse & Bate (2004), because the former allows larger timesteps to be taken. To advance a time-dependent variable A , from time $t = n$ to $t = n + 1$, the backwards Euler scheme states

$$A_i^{n+1} = A_i^n + dt \left(\frac{dA_i}{dt} \right)^{n+1}. \quad (17)$$

For a Gauss-Seidel method involving interactions between particles i and j , the new value A_i^{n+1} can be solved for by arranging the implicit equations into the form

$$A_i^{n+1} = \frac{A_i^n - dt \sum_j \sigma_{ij} (A_j^{n+1})}{1 - dt \sum_j \sigma_{ij}}, \quad (18)$$

where σ_{ij} contains quantities other than A , and A_j^{n+1} begins as A_j^n and is updated as soon as new values become available. This equation is iterated over until convergence is achieved.

The backwards Euler form of equation 14 is given by

$$\xi_i^{n+1} = \xi_i^n + dt \sum_j \frac{m_j}{\rho_i \rho_j} bc (\rho_i \xi_i^{n+1} - \rho_j \xi_j^{n+1}) \frac{\nabla W_{ij}}{r_{ij}} - dt (\nabla \cdot \mathbf{v})_i f_i \xi_i^{n+1} - dt ack_i \left[\frac{\rho_i \xi_i^{n+1}}{a} - \left(\frac{u_i^{n+1}}{c_{v,i}} \right)^4 \right], \quad (19)$$

where

$$b = \left[\frac{4 \frac{\lambda_i}{\kappa_i \rho_i} \frac{\lambda_j}{\kappa_j \rho_j}}{\left(\frac{\lambda_i}{\kappa_i \rho_i} + \frac{\lambda_j}{\kappa_j \rho_j} \right)} \right] \quad (20)$$

for brevity, and of equation 15 as

$$u_i^{n+1} = u_i^n + dt \sum_j \frac{1}{2} m_j \mathbf{v}_{ij} \cdot \nabla W_{ij} \left(\frac{u_i^{n+1} (\gamma - 1)}{\rho_i} + \frac{u_j^{n+1} (\gamma - 1)}{\rho_j} + \Pi_{ij} \right) + dt ack_i \left[\frac{\rho_i \xi_i^{n+1}}{a} - \left(\frac{u_i^{n+1}}{c_{v,i}} \right)^4 \right], \quad (21)$$

substituting in $(\gamma - 1)u\rho$ for p using our equation of state. These equations can be rearranged into the form of equation 18 to solve for ξ_i^{n+1} and u_i^{n+1} and Gauss-Seidel iteration performed with all other independent variables fixed.

We investigated two different approaches to solving these equations. The first method was to iterate over the Gauss-Seidel form of equations 19 and 21 separately but within the same iterations. This resulted in implicit integration that was many times faster than that of Whitehouse & Bate (2004) in optically thin regimes, but in optically thick regions the performance of the code was similar to that of Whitehouse & Bate (2004). The method also failed to converge for large timesteps when the energy transfer term (the last terms in equations 19 and 21) became large (due to high κ or large temperature differences between the gas and the radiation).

By far the most effective method is to solve equations 19 and 21 simultaneously for u_i^{n+1} , and to perform Gauss-Seidel iteration on the resulting expression. The resulting value of u_i^{n+1} is then substituted into equation 19 to obtain ξ_i^{n+1} during the same iteration. To simplify the subsequent equations we define the following quantities:

$$\begin{aligned} \beta &= dt \, c \, \kappa_i \, \rho_i, \\ \Gamma &= a \, c \, \kappa_i / c_{v,i}^4, \\ D_{d,i} &= \sum_j \frac{m_j}{\rho_j} c \, b \frac{\nabla W_{ij}}{r_{ij}}, \\ D_{n,i} &= - \sum_j \frac{m_j}{\rho_i \rho_j} c \, b \frac{\nabla W_{ij}}{r_{ij}} \rho_j \xi_j^{n+1}, \\ P_{d,i} &= \sum_j \frac{1}{2} m_j \mathbf{v}_{ij} \cdot \nabla W_{ij} \frac{(\gamma - 1)}{\rho_i}, \\ P_{n,i} &= \sum_j \frac{1}{2} m_j \mathbf{v}_{ij} \cdot \nabla W_{ij} \left[\frac{(\gamma - 1) u_j^{n+1}}{\rho_j} + \Pi_{ij} \right], \\ R_{p,i} &= (\nabla \cdot \mathbf{v})_i f_i, \\ \chi &= dt D_{d,i} - dt R_{p,i}. \end{aligned}$$

Using these new variables we can solve equation 21 for ξ_i^{n+1}

$$\xi_i^{n+1} = \frac{1}{\beta} \left(u_i^{n+1} - u_i^n - dt P_{n,i} - dt P_{d,i} u_i^{n+1} + dt \Gamma \left[u_i^{n+1} \right]^4 \right). \quad (22)$$

The right hand side of equation 22 then replaces ξ_i^{n+1} in equation 19, forming a quartic equation in u_i^{n+1} . If the quartic equation is cast in the form $a_4 x^4 + a_3 x^3 + a_2 x^2 + a_1 x + a_0 = 0$ then the co-efficients are given by:

$$\begin{aligned} a_4 &= \Gamma dt (\chi - 1) \\ a_3 &= 0 \\ a_2 &= 0 \\ a_1 &= (\chi - \beta - 1)(1 - dt P_{d,i}) \\ a_0 &= \beta \xi_i^n + (\chi - \beta - 1)(-u_i^n - dt P_{n,i}) + dt D_{n,i} \beta \end{aligned}$$

Solving this quartic equation yields a value for u_i^{n+1} , which may then be substituted into

$$\xi_i^{n+1} = \frac{\left(\xi_i^n + dt D_{n,i} + dt \Gamma \left[u_i^{n+1} \right]^4 \right)}{1 - \chi + \beta}, \quad (23)$$

using the quantities defined above (for the analytic solution of a quartic equation, see Appendix A of Whitehouse & Bate 2004). These solutions for ξ_i^{n+1} and u_i^{n+1} are iterated until they converge.

2.3 Prediction of position, density and smoothing length

We found that the accuracy when taking large implicit timesteps could be improved by predicting forward many of the quantities on the right-hand sides of equations 19 and 21 to time $t = n + 1$. The quantities x , ρ , and h can be predicted forwards as

$$\begin{aligned} x_i^{n+1} &= x_i^n + dt \, v_i^n \\ \rho_i^{n+1} &= \rho_i^n - dt \, \rho_i^n (\nabla \cdot \mathbf{v})_i^n \\ h_i^{n+1} &= h_i^n + dt \, h_i^n (\nabla \cdot \mathbf{v})_i^n. \end{aligned} \quad (24)$$

The improvement in accuracy was especially apparent in the case of the supercritical shock (see section 3.4).

2.4 Convergence criteria

We define convergence as being when the values of u_i^{n+1} and ξ_i^{n+1} obtained from the m -th iteration satisfy equations 19 and 21 to a given tolerance (with all occurrences of u_i^{n+1} and ξ_i^{n+1} on the right-hand sides of these equations being evaluated from iteration $m - 1$). Thus, for example, we iterate until the fractional errors in ξ given by

$$\frac{\xi_i^{n+1,m} - \left(\xi_i^n + dt \sum_j \frac{m_j}{\rho_i \rho_j} bc \left(\rho_i \xi_i^{n+1,m-1} - \rho_j \xi_j^{n+1} \right) \frac{\nabla W_{ij}}{r_{ij}} - dt (\nabla \cdot \mathbf{v})_i f_i \xi_i^{n+1,m-1} - dt a c \kappa_i \left[\frac{\rho_i \xi_i^{n+1,m-1}}{a} - \left(\frac{u_i^{n+1,m-1}}{c_{v,i}} \right)^4 \right] \right)}{\xi_i^{n+1,m}}, \quad (25)$$

are within a certain tolerance, for which we have typically used 10^{-3} .

In the event that the method fails to converge, we split the timestep into two halves, and begin the iterations again, using the result of the first half timestep as the input to the second. If either fails, we split the timesteps by another factor of two and continue this way until the system converges, or it reaches some excessively small fraction of the original timestep, at which stage it is no longer computationally efficient to continue the calculation.

2.5 Timestep criteria

The integration of the hydrodynamic variables requires that the timesteps obey the Courant condition for the hydrodynamic processes. The usual hydrodynamical SPH timestep criteria are

$$dt_{\text{Courant},i} = \frac{\zeta h_i}{c_s + h_i |\nabla \cdot \mathbf{v}|_i + 1.2 (\alpha_v c_s + \beta_v h_i |\nabla \cdot \mathbf{v}|_i)}, \quad (26)$$

and

$$dt_{\text{force},i} = \zeta \sqrt{\frac{h_i}{|a_i|}}, \quad (27)$$

where we use a Courant number of $\zeta = 0.3$, unless otherwise noted, and a_i is the acceleration of particle i . The lesser of these two quantities gives the hydrodynamical timestep.

There is also an explicit timestep associated with the radiation hydrodynamics, described in detail in Whitehouse & Bate (2004). This timestep is typically much smaller than the hydrodynamical timestep, and the new implicit method enables us to forgo the use of smaller timesteps in favour of the large hydrodynamical timestep.

3 TEST CALCULATIONS

We have once again duplicated the tests done by Turner & Stone (2001), as we did in Whitehouse & Bate (2004), this time however using the new code. This code achieves the same or better accuracy than the code described in Whitehouse & Bate (2004). However, in the vast majority of cases (especially those involving moving fluids) the new code is significantly faster than the old one.

3.1 Heating and cooling terms

We tested the interaction between the radiation and the gas to check that the temperatures of the gas and the radiation equalise at the correct rate when $T_g \neq T_r$ initially. A gas in a domain 10 cm long with 100 particles was set up so that there was no velocity, with a density $\rho = 10^{-7} \text{ g cm}^{-3}$, opacity $\kappa = 0.4 \text{ cm}^2 \text{ g}^{-1}$, and $\gamma = \frac{5}{3}$ and $E = \xi \rho = 10^{12} \text{ ergs cm}^{-3}$. Two tests were carried out, one where the gas heated until it reached the radiation temperature, and one where it cooled. The first test had $e = u\rho = 10^2 \text{ ergs cm}^{-3}$, and the second $e = u\rho = 10^{10} \text{ ergs cm}^{-3}$. The boundaries of the calculation used reflective ghost particles.

This problem can be approximated in the case where the energy in the radiation is much greater than that in the gas by the differential equation

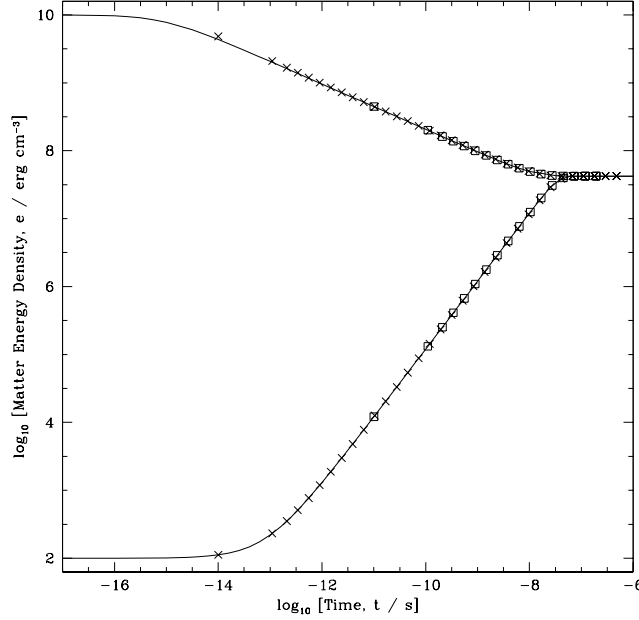


Figure 1. The evolution of the gas energy density e as it equilibrates with a radiation energy density $E = 10^{12} \text{ erg cm}^{-3}$. In the upper case, $e = 10^{10} \text{ erg cm}^{-3}$ initially, while in the lower case $e = 10^2 \text{ erg cm}^{-3}$. The solid line is the analytic solution, the crosses are the results of the SPH code using implicit timesteps of the lesser of 10^{-14} s or five percent of the elapsed time, and the squares with a timestep of the lesser of 10^{-11} s or five percent of the elapsed time. The symbols are plotted every ten timesteps.

$$\frac{de}{dt} = c\kappa E - ac\kappa \left(\frac{e}{\rho c_v} \right)^4, \quad (28)$$

and assuming E is constant.

In figure 1, the solid line is this analytic solution, plotted both for the cases where T_g increases and decreases. The crosses are the results of the SPH code using an implicit timestep that is set to the greater of 10^{-14} s or five percent of the time elapsed, similar to the way Whitehouse & Bate (2004) performed this test. The squares are similar, but with a timestep being the greater of 10^{-11} s or five percent of the time elapsed. As can be seen, the match between the analytic solution and the solutions given by the SPH code is once again excellent. On this test, the new method and that of Whitehouse & Bate (2004) are of comparable speed and each takes a few minutes.

3.2 Propagating radiation in optically thin media

In the standard diffusion approximation, in optically thin regions, radiation propagates at near infinite speed. This is unphysical, and the flux limiter has been introduced to limit the diffusion of radiation to the speed of light. To examine how well our code limits the speed of the radiation, a one centimetre long one-dimensional box is filled with 100 equally spaced SPH particles, with $E = 10^{-2} \text{ erg cm}^{-3}$ ($\xi = 0.4 \text{ erg g}^{-1}$), $\rho = 0.025 \text{ g cm}^{-3}$, and $\kappa = 0.4 \text{ cm}^2 \text{ g}^{-1}$. Initially, the radiation and gas are in thermal equilibrium.

At the start of the simulation, the radiation energy density for the leftmost ten particles was changed to $E = 0.1 \text{ erg cm}^{-3}$ ($\xi = 4 \text{ erg g}^{-1}$) causing a radiation front that was allowed to propagate across the region. The ghost particles were reflective except in specific radiation energy ξ , which was fixed equal to $\xi = 4 \text{ erg g}^{-1}$ at the left hand boundary and $\xi = 0.4 \text{ erg g}^{-1}$ at the right hand boundary. The implicit code was used with various timesteps ranging from an explicit timestep to a single implicit step lasting 10^{-11} s . The results are shown in figure 2.

As shown by the figure, the radiation pulse propagates at the correct speed, even using one single large timestep. The front is smoothed out in a manner similar to the results of Turner & Stone (2001) and Whitehouse & Bate (2004); both methods are quite diffusive in this situation. The new code is slower than that of Whitehouse & Bate (2004) for an explicit timestep, but superior for all longer timesteps.

3.3 Optically-thick (adiabatic) and optically-thin (isothermal) shocks

A shock-tube test, identical to the one in Whitehouse & Bate (2004), was set up to investigate the way the code simulated optically-thin and optically-thick regimes and the transition between them. In the limit of high optical depth, the gas cannot cool because the radiation is trapped within the gas; thus the shock is adiabatic. An optically-thin shock, on the other hand, is able to efficiently radiate away the thermal energy and thus behaves as an isothermal shock. In these shock tests, the gas and radiation are highly coupled and, thus, their temperatures are equal.

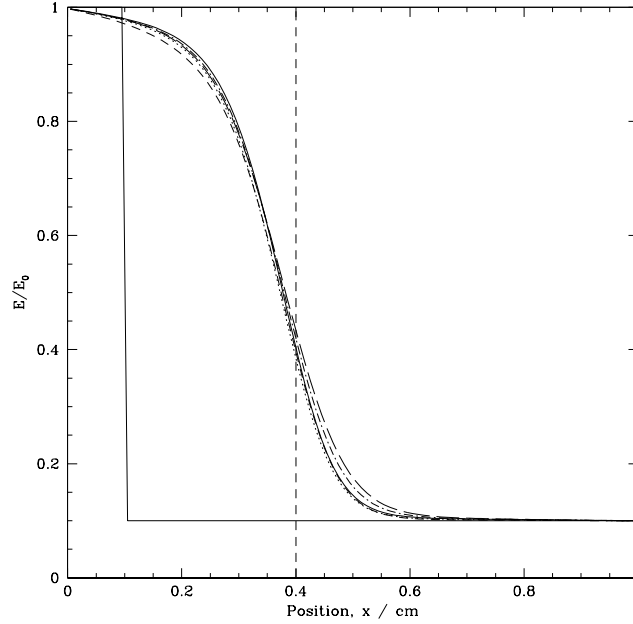


Figure 2. The propagation of a radiation pulse across a uniform medium. The time is $t = 10^{-11}$ s. The vertical dashed line shows the expected position of the pulse based on the speed of light. The results are almost independent of the size of the implicit timestep used. Results are given for implicit timesteps equal to (solid line), ten times (dotted line), one hundred times (short-dashed line), and one thousand times (long-dashed line) the explicit timestep. The dot-dashed line gives the result using a single implicit step of 10^{-11} s. The initial conditions are also shown as a solid line.

A domain 2×10^{15} cm long extending from $x = -1 \times 10^{15}$ to 1×10^{15} cm was set up, with an initial density of $\rho = 10^{-10}$ g cm $^{-3}$, and the temperatures of the gas and radiation were initially 1500 K. One hundred particles were equally spaced in the domain, with those with negative x having a velocity equal to the adiabatic ($\gamma = 5/3$) sound speed $v_0 = c_s = 3.2 \times 10^5$ cm s $^{-1}$, and those with positive x travelling at the same speed in the opposite direction. The two flows impact at the origin, and a shock forms. Opacities of $\kappa = 40, 0.4, 4.0 \times 10^{-3}$ and 4.0×10^{-5} cm 2 g $^{-1}$ were used to follow the transition from adiabatic to isothermal behaviour. Ghost particles were placed outside the boundaries and maintain the initial energies of their respective real particles. The boundaries moved inwards with the same velocity as the initial velocities of the two streams. These moving boundaries cause slight perturbations in the densities of those particles closest to the boundaries, however this does not affect the solution in the vicinity of the shocks.

The optically thick and thin limits can be solved analytically (e.g. Zel'dovich & Raizer 2002). The shock speed is given by

$$D = \frac{(\gamma_{\text{eff}} - 3) + \sqrt{(\gamma_{\text{eff}} + 1)^2 v_0^2 + 16\gamma_{\text{eff}}}}{4}, \quad (29)$$

where $\gamma_{\text{eff}} = 1$ for the isothermal case, and $\gamma_{\text{eff}} = 5/3$ for the adiabatic case. The ratio of the final to the initial density is given by

$$\frac{\rho_1}{\rho_0} = 1 + \frac{v_0}{D}, \quad (30)$$

and, for the adiabatic shock, the ratio of the final to the initial temperature is given by

$$\frac{T_1}{T_0} = \frac{\rho_1}{\rho_0} + \frac{v_0 D \rho_0}{p_0}. \quad (31)$$

These analytic solutions are shown by the solid and dashed lines in figure 3. In the figure, the opacity decreases from top to bottom showing the transition from optically-thick (adiabatic) to optically-thin (isothermal) behaviour. The extremes are in good agreement with their respective analytic adiabatic and isothermal solutions. Note that the spike in thermal energy near the origin and the corresponding reduction in density for the optically-thick case (due to ‘wall-heating’) is softened by the radiation transport that occurs in the intermediate opacity calculation with $\kappa = 0.4$.

In comparison to the code described in Whitehouse & Bate (2004), these shocks were many times faster. The timestep was limited by the hydrodynamical criteria only. The $\kappa = 40$ and $\kappa = 0.4$ shocks ran in less than a minute, compared to the old code which took thirty-four hours and thirty-five minutes, respectively. The $\kappa = 4 \times 10^{-3}$ shock took just under one minute, compared to forty-five minutes for the old code. The $\kappa = 4 \times 10^{-5}$ code took twenty-three minutes, compared to the previous time of ten hours.

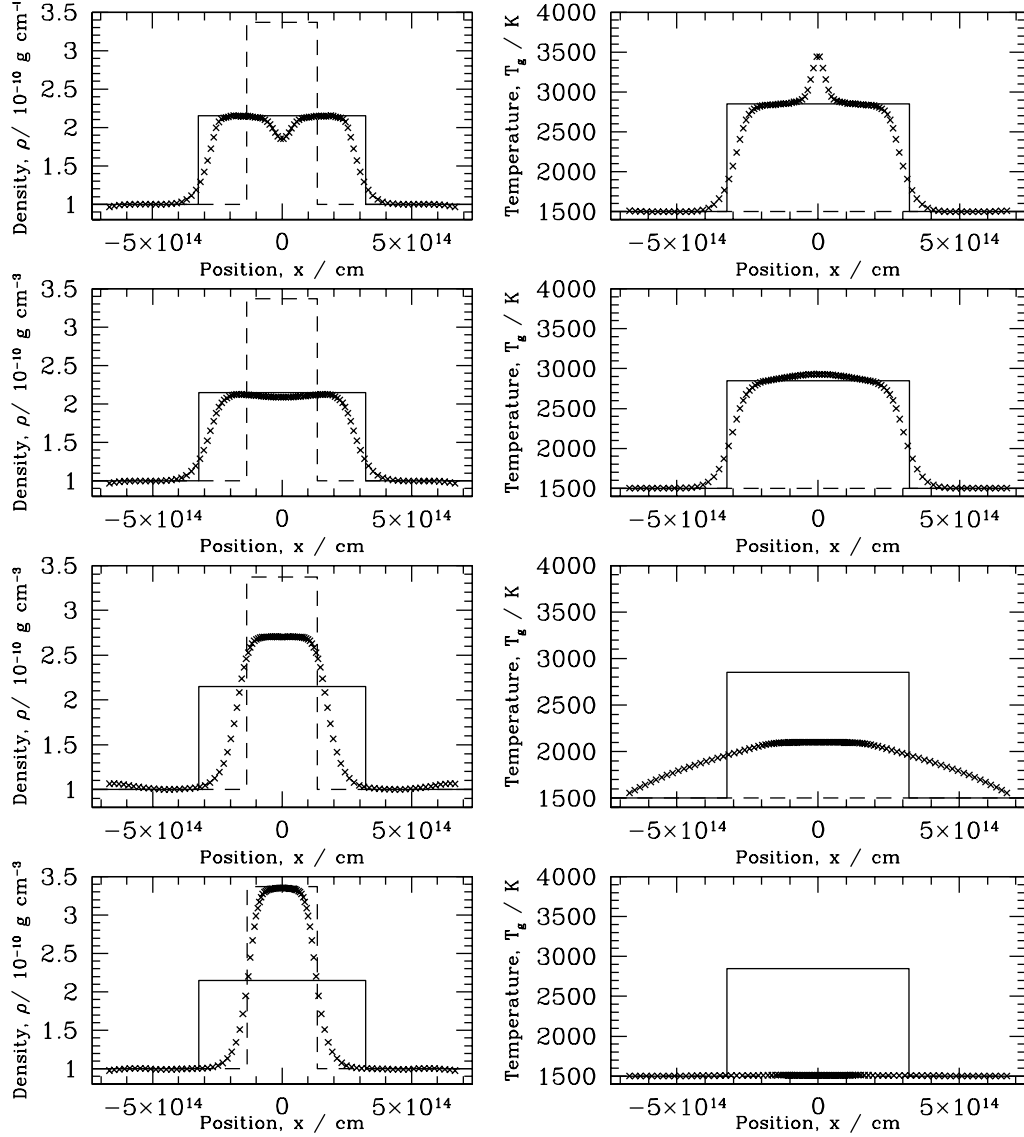


Figure 3. A set of shocks with differing opacity at time $t = 1.0 \times 10^9$ s. Density is on the left, and gas temperature on the right. The crosses are the SPH results; the solid line gives the analytic solution for an adiabatic shock, and the dashed line for an isothermal shock. The opacities are (top) $\kappa = 40$, (upper middle) $\kappa = 0.4$, (lower middle) $\kappa = 4.0 \times 10^{-3}$ and (bottom) $\kappa = 4.0 \times 10^{-5}$ $\text{cm}^2 \text{g}^{-1}$. As the opacity is decreased, the shocks transition from adiabatic to isothermal behaviour.

3.4 Sub- and super-critical shocks

A supercritical shock occurs when the photons generated by a shock have sufficient energy to preheat the material upstream. The characteristic temperature profile of a supercritical shock is where the temperature on either side of the shock is similar, rather than the downstream temperature being much higher than that upstream, as occurs in a subcritical shock (see Zel'dovich & Raizer 2002, for more details).

The initial conditions of this problem are those of Sincell, Gehmeyr & Mihalas (1999) and Turner & Stone (2001). A gas with opacity $\kappa = 0.4 \text{ cm}^2 \text{g}^{-1}$, uniform density $\rho = 7.78 \times 10^{-10} \text{ g cm}^{-3}$, mean molecular weight $\mu = 0.5$ and $\gamma = \frac{5}{3}$ is set up with ξ and u in equilibrium, with a temperature gradient of $T = 10 + (75x/7 \times 10^{10}) \text{ K}$. Initially the particles are equally spaced between $x = 0$ and $x = 7 \times 10^{10} \text{ cm}$ for the supercritical shock, and between $x = 0$ and $x = 3.5 \times 10^{10} \text{ cm}$ for the subcritical shock. At time $t = 0$ a piston starts to move into the fluid from the left-hand boundary (simulated by moving the location of the boundary). For the subcritical shock the piston velocity is $v_p = 6 \text{ km s}^{-1}$, and for the supercritical shock $v_p = 16 \text{ km s}^{-1}$, as per Sincell et al. (1999). The ghost particles are reflective in the frame of reference of the boundary. Artificial viscosity parameters $\alpha_v = 2$ and $\beta_v = 4$ were used to smooth out oscillations.

The results of calculations for a sub-critical shock (piston velocity $v_p = 6 \text{ km s}^{-1}$) are shown in figure 4. The top left panel for each shows the temperature of the radiation field (solid line) and the gas (dotted line) against position, and the top right shows the same quantities against optical depth τ , with $\tau = 0$ set at the shock front (measured from the density distribution). The bottom left panel shows normalised flux, and the bottom right the value of the Eddington factor. The analytic solutions discussed by Sincell et al. (1999) and Zel'dovich & Raizer

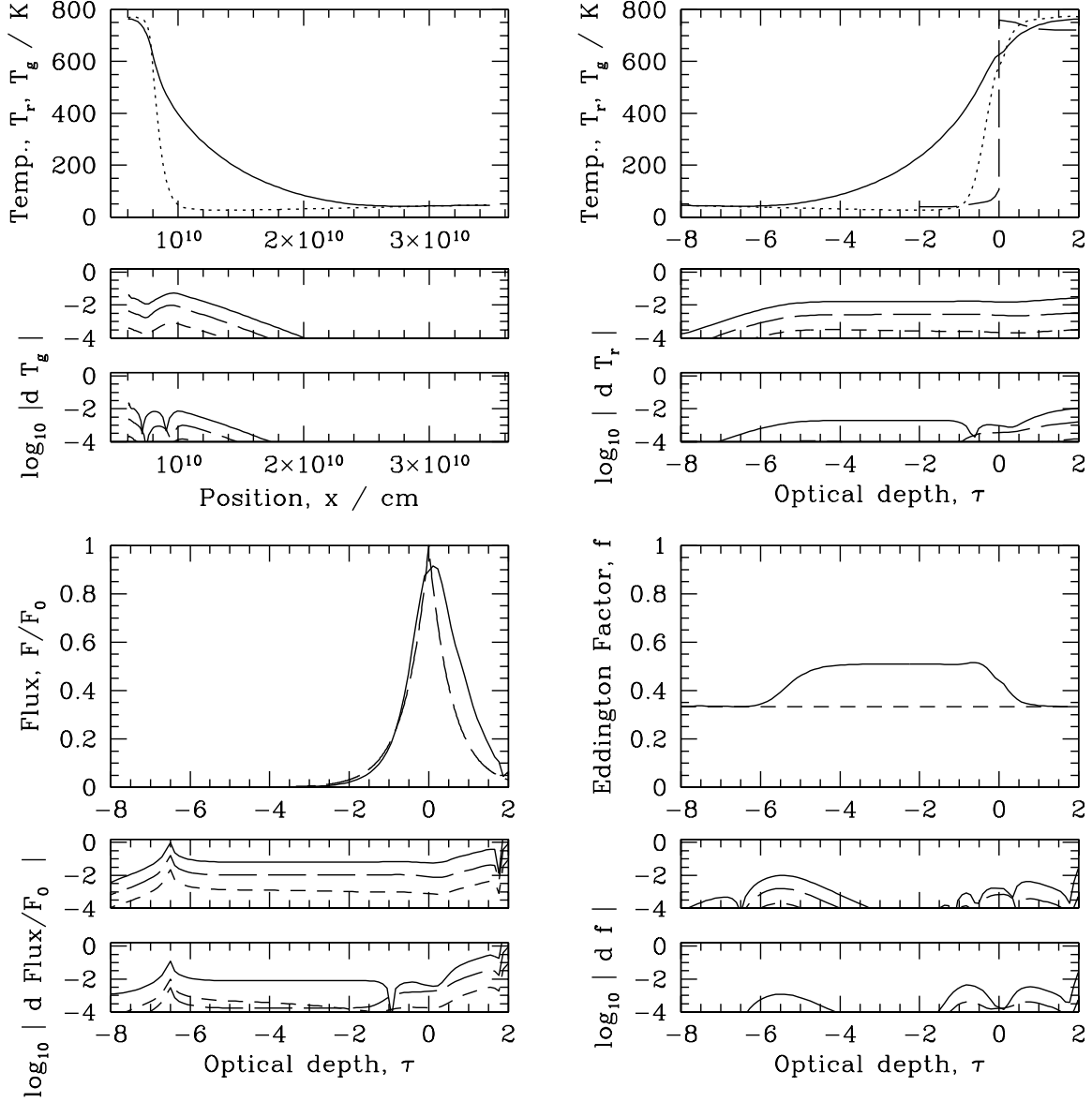


Figure 4. The sub-critical shock with piston velocity $6 \times 10^5 \text{ cm s}^{-1}$ and 100 particles. The large panels show the results using the explicit code. The top panels show radiation (solid line) and gas (dotted line) temperatures. The bottom left panel shows the normalised flux and bottom right panel the Eddington factor. The long-dashed lines give the analytic solutions for the gas temperature and normalised flux. An Eddington factor of $1/3$ is also indicated for reference (short-dashed line, lower right panel). The subpanels plot the logarithm of the difference between the results using the explicit code and the implicit code (see the main text). The subpanels show the results with (lower subpanel) and without (upper subpanel) predicting x, h and ρ forwards in time. The implicit code was run with timesteps one times (solid line), one tenth of (long-dashed line) and one hundredth of (short-dashed line) the *hydrodynamic* timestep.

(2002) for the temperatures and fluxes of the shocks are shown with long-dashed lines. Figures 4 and 5 are plotted using the explicit code. In subpanels beneath the main panels, we compare the results from the implicit code with the explicit results. Calculations were performed using the implicit code with timesteps of one, one tenth and one hundredth the hydrodynamical timestep criteria. In the subpanels, we plot the differences of the implicit results with respect to the explicit results. We divide the difference between the implicit and explicit values by the explicit value to obtain a fractional error and take the logarithm of the absolute value of this fraction. Thus, a difference of -2 on the subpanels corresponds to an error of 1 percent with respect to the explicit result. The subpanels in figure 4 shows the log fractional error of an implicit code with (bottom subpanels) and without (top subpanels) the prediction of x, h and ρ discussed in section 2.3. Similarly, figure 5 show the super-critical shock in the same way, excluding (top) and including (bottom) the prediction mentioned in section 2.3. The prediction of x, h and ρ makes the sub-critical shock significantly more accurate for hydrodynamical timesteps, whilst having a smaller benefit for the super-critical shock. Figure 6 shows how increasing the resolution of the simulation enables us to resolve the spike in gas temperature at the shock front in a super-critical shock.

The new implicit method is many times faster than the old method. In Whitehouse & Bate (2004), the super-critical shock with the

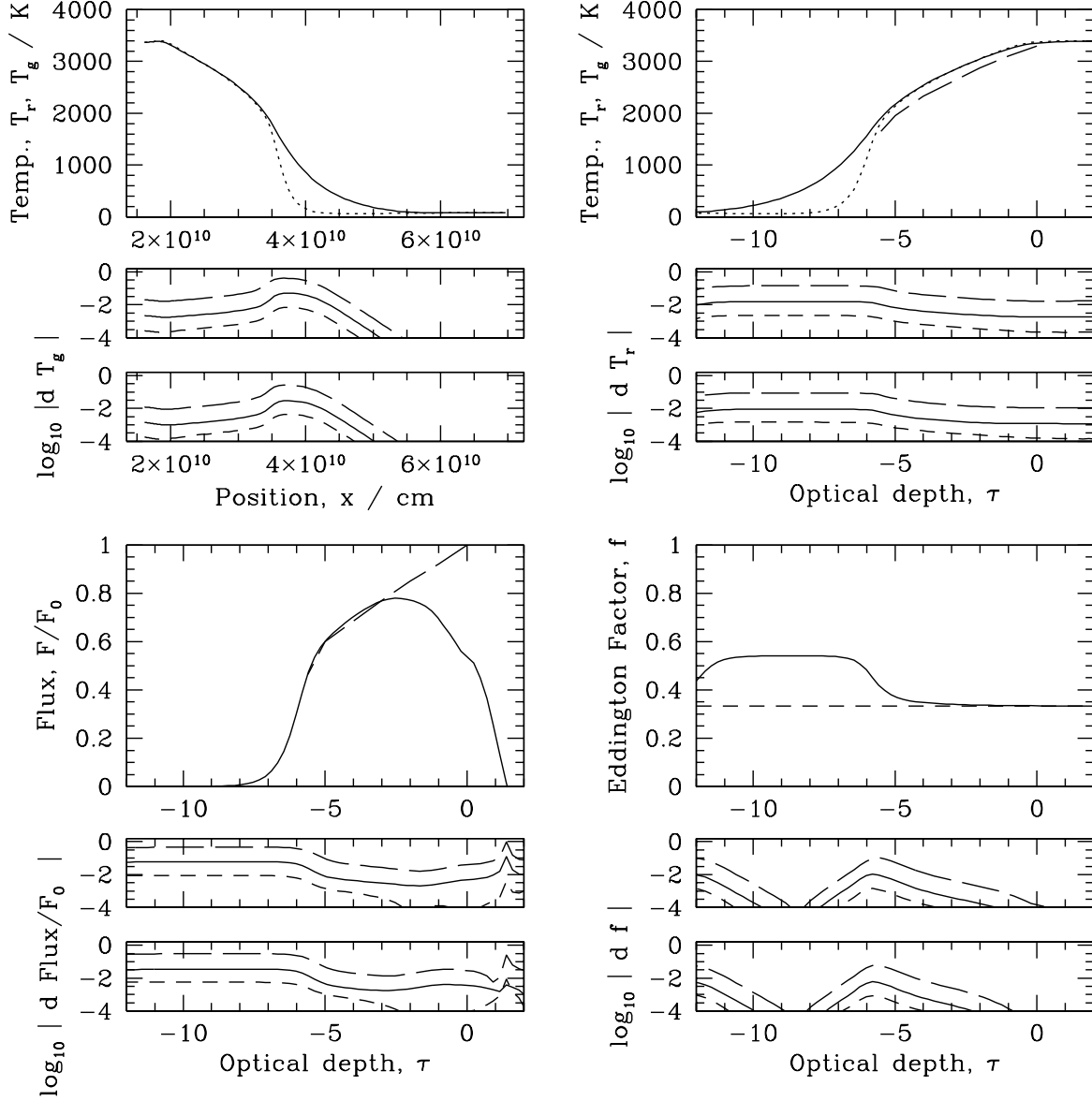


Figure 5. The super-critical shock, with piston velocity $1.6 \times 10^6 \text{ cm s}^{-1}$, 100 particles. The subpanels shown the results with (bottom) and without (top) predicting x, h and ρ forwards in time. This shock is strong enough for radiation from the shock to preheat the gas upstream. See figure 4 for details of the line meanings.

hydrodynamic timestep criteria took nearly ten days. The new code performed the same calculation on a comparable CPU in two minutes, making the new algorithm approximately 10^4 times faster. A similar improvement in performance can be seen with the sub-critical shock – the hydrodynamic timestep run took over twenty-three days for Whitehouse & Bate (2004), while the present method ran in four minutes, yielding an increase again of $\approx 10^4$ times.

3.5 Radiation-dominated shock

In material of high optical depth the radiation generated in a shock cannot diffuse away at a high rate, and so the radiation becomes confined in a thin region adjacent to the shock. Turner & Stone (2001) performed a calculation that tests whether the shock thickness is what one would expect in these circumstances. An extremely high Mach number shock (Mach number of 658) is set up, with the gas on the left having an initial density of $\rho = 0.01 \text{ g cm}^{-3}$, opacity $\kappa = 0.4 \text{ cm}^2 \text{ g}^{-1}$, temperature $T_r = T_g = 10^4 \text{ K}$, and speed 10^9 cm s^{-1} . The gas on the right has density $\rho = 0.0685847 \text{ g cm}^{-3}$, opacity $\kappa = 0.4 \text{ cm}^2 \text{ g}^{-1}$, temperature $T_r = T_g = 4.239 \times 10^7 \text{ K}$, and speed $1.458 \times 10^8 \text{ cm s}^{-1}$. The density contrast is set initially by using different mass particles, however as the simulation evolves particles from the left enter the shock and by the time the figure is plotted all the particles shown have the same mass. The locations of the boundaries move with the same speed as their

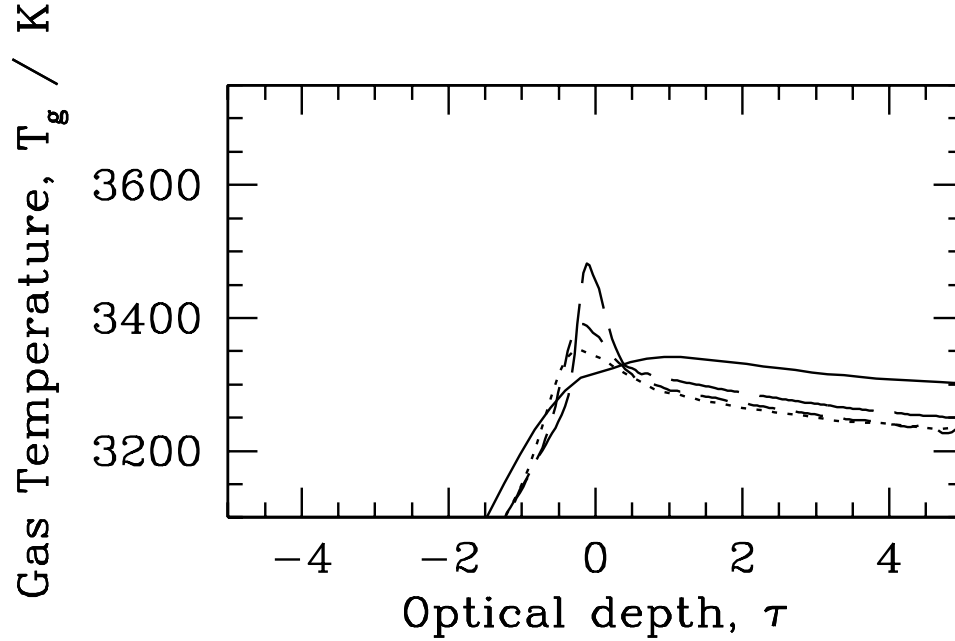


Figure 6. The super-critical shock, with piston velocity 16 km s^{-1} , showing how changing the resolution affects the spike in gas temperature at the shock. All calculations use a hydrodynamical timestep and the implicit code. The solid line is with 100 particles, the dotted line with 200 particles, and the long-dashed with 500 particles. The short-dashed line shows the results with 500 particles and double the number of neighbours (16 instead of 8).

respective particles, and the properties of the ghost particles outside these boundaries are fixed at their initial values. We use hydrodynamical timestep with a Courant number of $\zeta = 0.03$. 1500 particles are equally spaced over a domain extending from $x = -6 \times 10^5 \text{ cm}$ to $x = 1.5 \times 10^5 \text{ cm}$ initially, with the discontinuity at $x = 0.5 \times 10^5 \text{ cm}$. The location of the shock should be fixed in this frame, although individual particles flow through the shock.

After a period where a transient feature forms at the shock front and drifts downstream with the flow, a stable shock is established. Its thickness is expected to be roughly equal to the distance $l = c\lambda/k\rho u_1$, where u_1 is the speed of material flowing into the shock front.

Figure 7 shows the results at a time $t = 5 \times 10^{-4} \text{ s}$, of the radiation energy density E , gas energy density e , velocity v , and density ρ versus position. The vertical dashed lines indicate the expected shock thickness and the SPH results are in good agreement. The after-effects of the transient moving downstream can again be seen on the right of the plots of density and gas energy density. Whitehouse & Bate (2004) were unable to run this test case with the large timestep used here because it required an unacceptable amount of computational time. The calculation presented here required approximately a week.

4 CONCLUSIONS

We have presented a more efficient method for performing radiative transfer in the flux-limited diffusion approximation within the SPH formalism. This gives a speed increase of many thousand times over the code of Whitehouse & Bate (2004). In every test, the new implicit code is much faster than the old code for large implicit timesteps, with no loss in accuracy.

Whilst the method described here is presented in one dimension, the addition of the algorithm into a three-dimensional code is easily accomplished. The major difference between the one- and three-dimensional algorithms is the form of the radiation pressure, which involves a more complicated tensor equation. We are performing simulations in three dimensions using this algorithm which will be published in due course.

ACKNOWLEDGMENTS

SCW acknowledges support from a PPARC postgraduate studentship. MRB is grateful for the support of a Philip Leverhulme Prize.

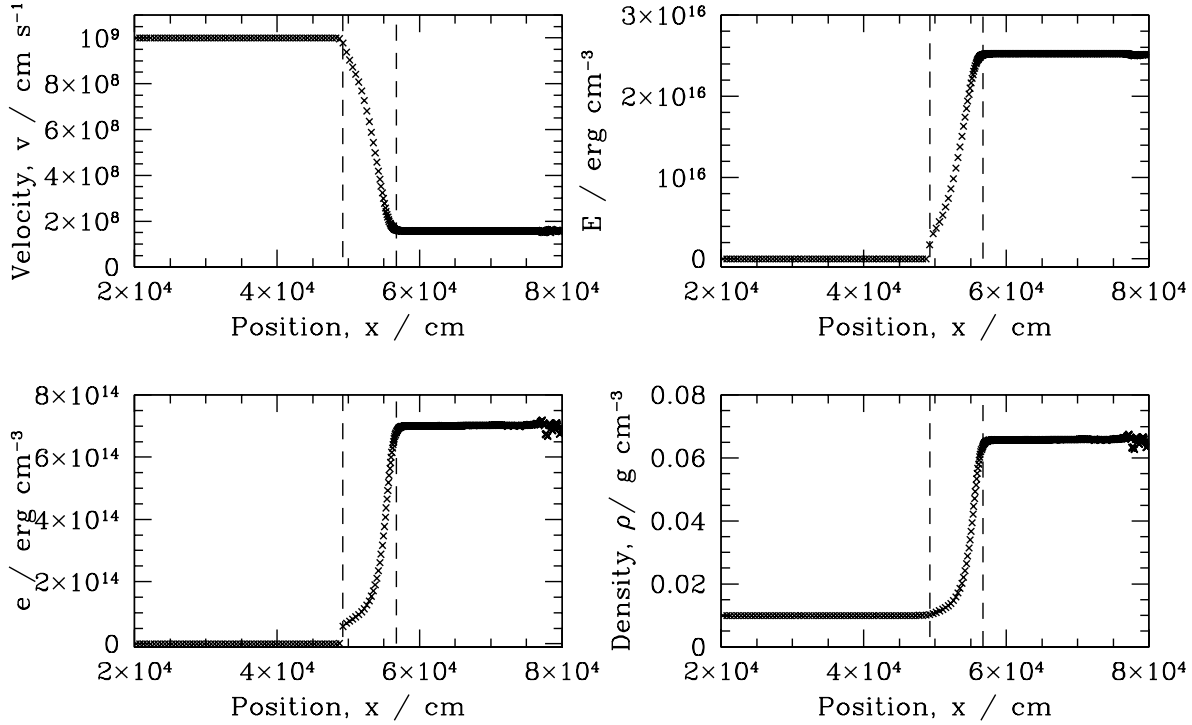


Figure 7. The radiation-dominated shock at time $t = 5 \times 10^{-4}$ s. We plot the velocity, radiation and gas energy densities and gas density versus position. The vertical dashed lines show the expected shock thickness. Gas flows into the shock from the left. The after effects of the transient that occurs at the start of the calculation can be seen at the far right of the plots.

REFERENCES

- Bastien P., Cha S.-H., Viau S., 2004, in *Revista Mexicana de Astronomia y Astrofisica Conference Series SPH with radiative transfer: method and applications*. pp 144–147
- Brookshaw L., 1985, *Proceedings of the Astronomical Society of Australia*, 6, 207
- Brookshaw L., 1986, *Proceedings of the Astronomical Society of Australia*, 6, 461
- Gingold R. A., Monaghan J. J., 1977, *MNRAS*, 181, 375
- Levermore C. D., Pomraning G. C., 1981, *ApJ*, 248, 321
- Lucy L. B., 1977, *AJ*, 82, 1013
- Mihalas D., Mihalas B. W., 1984, *Foundations of Radiation Hydrodynamics*. Oxford University Press
- Monaghan J. J., 1992, *Ann. Rev. Astron. Astrophys.*, 30, 543
- Oxley S., Woolfson M. M., 2003, *MNRAS*, 343, 900
- Sincell M. W., Gehmeyr M., Mihalas D., 1999, *Shock Waves*, 9, 391
- Turner N. J., Stone J. M., 2001, *ApJS*, 135, 95
- Viau, S. 1995, *Doctoral thesis*, University of Montreal
- Whitehouse S. C., Bate M. R., 2004, *MNRAS*, 353, 1078
- Zel'dovich Y. B., Raizer Y. P., 2002, *Physics of Shock Waves and High-Temperature Hydrodynamic Phenomena*, edited Hayes and Probstein. Dover, New York